Design of the high-payload flapping wing robot E-Flap

Raphael Zufferey, Jesús Tormo-Barbero, M. Mar
Guzmán, Fco. Javier Maldonado, Ernesto Sanchez-Laulhe, Pedro Grau, Martín Pérez, José Ángel Acosta, Anibal Ollero[1]

***Abstract*—Autonomous lightweight flapping-wing robots show potential to become a safe and affordable solution for rapidly deploying robots around humans and in complex environments. The absence of propellers makes such vehicles more resistant to physical contact, permitting flight in cluttered environments, and collaborating with humans. Importantly, the provision of thousands of species of birds that have already mastered the challenging task of flapping flight is a rich source of solutions. However, small wing flapping technology is still in its beginnings, with limited levels of autonomy and physical interaction capability with the environment. One significant limitation to this is the low payload available. Here we show the Eagle-inspired Flapping-wing robot E-Flap, a 510g novel design capable of a 100% of payload, exceeding the requirement of the computing and sensing package needed to fly with a high degree of autonomy. The concept is extensively characterized, both in a tracked indoor space and in outdoor conditions. We demonstrate flight path angle of up to 50°and velocities from as low as 2 m/s to over 6m/s. Overall, the robotic platform has been proven to be reliable, having performed over 100 flights. Through mechanical and electronics advances, the E-Flap is a robust vehicle prototype and paves the way towards flapping-wing robots becoming a practical fully autonomous flying solution. Video attachment: https://youtu.be/GpAa176TMf0.**

Figure 1. Front view of the flying E-Flap robot during a downstroke.

I. Introduction

Flapping-wing robots leverage a bio-inspired method to solve the challenges of aerial flight. Through the use of rapidly oscillating wings, a vehicle can generate enough lift and thrust to both move forward and sustain its weight. Flapping-wing technology removes the requirements of additional thrust producing engines, traditionally based on fast rotating propellers. This significantly reduces the hazards of most small flying crafts to humans and structures and reduces the perceived threat. In addition, flapping wings can be much quieter thanks to the lack of high-velocity noisy surfaces, and more importantly, do not tend to break easily upon impacting with structures. The latter makes flapping-wing vehicles particularly interesting for studying perching situations, where impacts are likely to happen. Moreover, this tolerance for physical interaction with the environment opens the door to performing flights in close proximity to humans and animals, as well as intermittent flight with landing and take-off. Altogether, flapping-wing robots are an extremely promising technology to perform safe, robust and affordable aerial flights.

However, flapping flight presents a formidable challenge, which continues to hinder the development of such robots for real-world applications. Structurally, the movement of wings at the 1 kg weight range is slow (compared to propellers) but necessitates high torques, posing substantial design challenges for the structure and the drive transmission. Aerodynamically, the airflow over a flapping wing is highly turbulent, rendering modeling and control of such robots difficult. Lastly, a purely oscillating wing generates insufficient thrust, demanding an additional wing twisting mechanism, either active or passively-induced through elasticity. While parts of these challenges have been addressed with innovative solutions and methods, the ability of flapping-wing robots to physically interact with the environment and with humans is still quite limited.

In recent years, groundbreaking flapping-wing robots, also known as ornithopters, have been proposed at the small scale. Their design is inspired by insects at the milli-gram scale, such as the Robobee [1], and by small birds or bats at the gram scale as the KuBeetle-S [2] and the BatBot [3]. An important feature shown in small, gram-scale ornithopters is the hovering capability that is achieved by design, facilitating landing and precise positioning [4]. While the engineering and the design of those ornithopters is certainly impressive, their use in real-world applications is limited, mainly due to the lack of additional payload that degrades both their computational power and flight time. Nevertheless, as it is well known, extrapolating these designs to a larger scale is difficult due to their different operating regimes, as e.g. Reynolds number and structural stress.

Good examples of medium-scale ornithopters are the Dove [5] and ThunderI [6], ranging between 200 - 350g and with half-meter wingspan. Both have a similar velocity (around 10 m/s). The Dove boasts a state-of-the-art 100g payload which is employed to carry its custom electronics and a camera for one specific flight mission and therefore the additional payload is quite limited.

At a larger scale, maximum speed and payload capabilities are further enhanced as exemplified by the RoboRaven. This project consists of several robot variants (RoboRaven I–IV [7], [8]). The RoboRaven (200-700g) has shown flight speeds of down to $6\,\mathrm{m/s}$ and an unique design with on-board solar panels capable

Manuscript received: October 15, 2020; revised: January 8, 2021; accepted: February 3, 2021.

This paper was recommended for publication by Editor Xinyu Liu upon evaluation of the Associate Editor and Reviewers comments. This work was supported by the European Project GRIFFIN ERC Advanced Grant 2017, Action 788247.

[1]All the authors are with the GRVC, University of Seville, Spain. Corresponding author: raph.zufferey@gmail.com.

Digital Object Identifier (DOI): see top of this page.

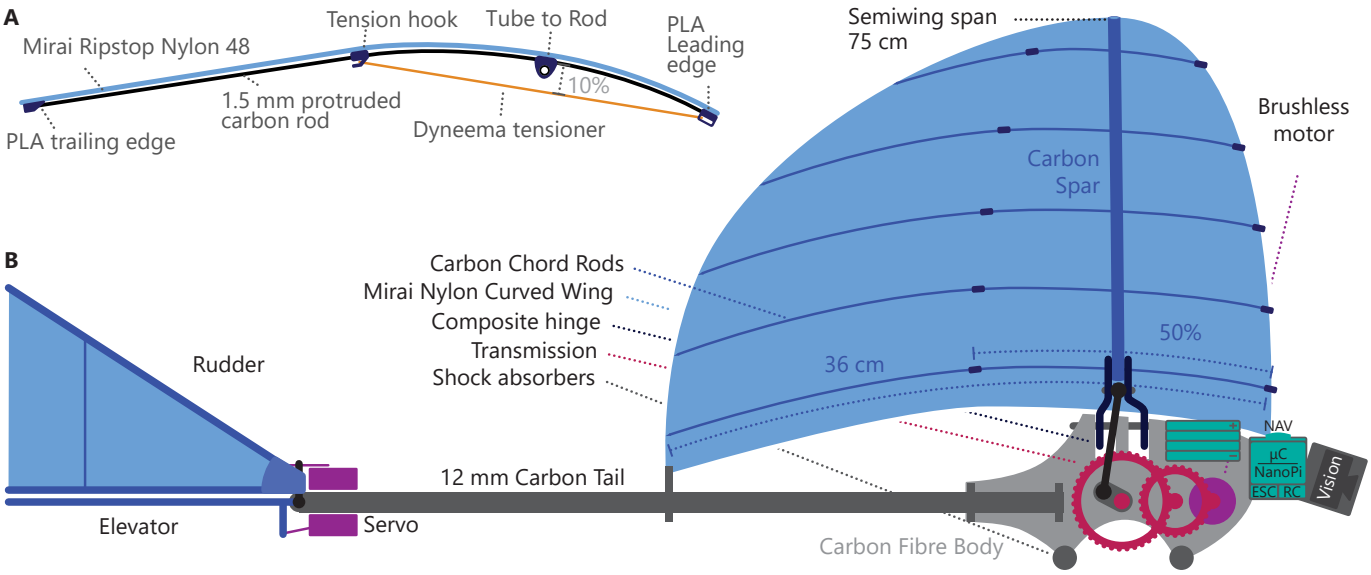

Figure 2. Schematic of the robotic bird with its wing in upwards position.

of supplying almost half of the power required in flight. On the other hand, the bio-inspired Robird Falcon exhibits a higher flight velocity of about 16 m/s as it has been designed specifically to deter birds in airports. Lastly, the RoBird Bald Eagle (2.1kg) [9] and Festo Smart Bird (450g) [10] are among the largest ornithopters with a wingspan around $150\,\mathrm{cm}$. The Robird Bald Eagle is reported to have a 1kg payload, bringing the total weight to 3.1kg (33 % of its weight) and flight speed of 18 m/s, and the Smart Bird is designed as a remotely piloted science demonstrator. While those large robots are excellent demonstrators or bird-deterrents, they are not designed to perform physical interaction with the environment, which requires high computational power and low flight speeds.

In summary, all of those previous designs meet the requirements for what they were made. However, physical interaction were not included among those requirements and the E-Flap robot proposed here has been specifically designed for that. Thus, E-Flap is a novel flapping-wing robot dotted with powerful elastic wings allowing for extra payload, interaction capability and autonomy. Its optimized ultra-light electronic architecture is also presented, unifying the low-level drivers with a linux-based companion computer. Fig. 2.B shows a side view representation of the robot highlighting broad structure, design and disposition choices.

The E-Flap has been developed within the GRIFFIN[i] Advanced Grant of the European Research Council, that includes the following features: (1) Robotic system with autonomous capabilities, which means not only control but also on-board perception and planning capabilities; (2) Manipulation capability to perform physical tasks. These capabilities are new for flapping-wing robots and had not been covered by existing ornithopters. The E-flap is a preliminary prototype, still without manipulation capabilities but with the characteristics to be evolved into an aerial manipulation system. It was developed to meet the following challenging requirements never achieved jointly up to now:

- Hardware and computational power needed to perform on-board reliable perception, including an event camera, for future autonomous operation to fly Beyond Visual Line of Sight safely.
- 0.5 kg total empty weight and a 100% of additional payload, permitting on-board manipulation capabilities.
- Minimum flight velocity of 2 m/s to physically interact with the environment, with autonomous on-board perception
- Maximal wing span of 1.5 m in order to fly in the existing testbed with accurate indoor positioning to validate flight and perching performances repeatedly.
- A robust and modular design to adapt to multiple science experiments.

The proposed 510 grams prototype meets those requirements and features a double elliptical symmetric wing with a total span of $1.5\,\mathrm{m}$ that offers low flight speeds from $2\,\mathrm{m/s}$ up to $6\,\mathrm{m/s}$. The platform is capable of carrying a payload of up to $520\,\mathrm{g}$, equivalent to 100% of its own weight (see sec. V-B). Moreover, the robot has withstood 94 active flights indoors and outdoors with minor damage, even as most flights ended in impacts with the ground or structures. The E-Flap carries custom electronics that runs the indoor flight controller and that will also enable a high level of autonomy outdoors in a compact and lightweight package.

This research article contributes to the field of aerial robotics with a new payload-capable flapping-wing design, validated by thorough experiments. The technological innovation resides in: a) a rapid structure manufacturing method, relying almost exclusively on standard lab equipment, opening up applications and replication in any robotics labs; b) a lightweight integrated electronic framework that will permit autonomous flights; c) a new wing skeleton with optional camber; and d) a modular design for the structure, wings and the tail. Lastly, we validate the design both in a controlled, tracked zone and in outdoor conditions. We show that the vehicle is robust, easily repairable, with high maneuverability. This robot is the result of a prototyping methodology spanning over a year of optimization and game-changing payload improvements from previous studies [11].

This paper is structured in two main parts. First, the design process of the E-Flap is presented Sec. II, along with powertrain estimations in Sec. III and electronics developments in Sec. IV. The resulting robot is validated through indoor tracked experiments (Sec. V) and outdoor manual flights (Sec. V-F). This research lays

[i]General compliant aerial Robotic manipulation system Integrating Fixed and Flapping wings to INcrease range and safety (https://griffin-erc-advanced-grant.eu).

the foundation for full autonomy and practical physical interaction tasks with flapping-wing robots.

II. Structural Design Development

This section discuss the design choices that led up to the characteristic design of E-Flap, whose main specifications are summed up in Table I.

Table I
E-Flap main specifications

Parameter	Value	Description
m	0.510 kg	Mass (w/ battery, w/o payload)
S	0.438 m^2	Wing surface
b	1.5 m	Wingspan
S_t	0.099m^2	Tail surface
Φ	30-50 deg	Flapping amplitude
D	5 deg	Mean dihedral angle
f	5.5 Hz	Maximum flapping frequency
K_v	1130 rpm/V	Brushless motor K_v constant
V	16.5 V	Battery voltage
C	450 mAh	Battery capacity

A. Aero-elastic Wings

The wings are perhaps the most critical element of a flapping-wing robot. They undergo high torque at the root, are often the first element to impact on landing yet need to be extremely lightweight to minimize the flapping inertia.

The ornithopter design has been done with maximum payload as criteria, which increases with the size of the robot. However, a large ornithopter suffers from reduced maneuverability and requires large flight spaces. We bound the wingspan to 1.5m, which is the maximum possible in the indoor testbed. The total design mass is 1kg, which combines a 500g robot weight and a 100% payload, based on [5]. The wing area is estimated to $0.5\,m^2$ from the steady level powered flight equation: $\rho C_L v^2 S = 2Mg$ with the total mass M, the gravity g, the lift coefficient $C_L = 1.3$ from CFD and a target flight velocity of $v = 5\,m/s$. Flapping wings benefit from elliptical wing shapes. Not only do they reduce wing tip losses, they also reduce wing inertia by concentrating more weight near the wing root. The actual wing shape is close to an elliptical chord distribution maintaining a $\frac{1}{4}$ chord alignment. The chord distribution is selected to keep an aspect ratio of $b^2/S = 5$, resulting in a $0.36\,m$ root chord and $0.29\,m$ mean chord.

The E-Flap relies on a proven method for producing a reliable wing in less than 3 hours with only standard 3D-printing equipment. The resulting wing weighs 82 gram for a 1.5 m wingspan and 36 cm chord or only 55 gram per meter. The skeleton of the wing is light thanks to its extensive use of composite materials. It is composed of a $6\,mm$ woven CF tube spar intersected orthogonally by $1.5\,mm$ CF rods every $15\,cm$, held in place by 3D-printed ring connectors. The nylon ripstop fabric covers the skeleton as displayed in light blue in Fig. 1.B. This $48\,g/m^2$ fabric is highly tear resistant, can be glued with cyanoacrilate glue or bonded with ripstop tape.

The wing features an optional camber (Fig. 2.A) along the whole wing yet maintains a flexible trailing edge, improving thrust. The camber is fixed by a removable Dyneema loop (an UHMWPE fiber exhibiting extremely high strength-to-weight ratio) as shown in Fig. 2.A. The leading edge part inserts over the carbon-fiber (CF) rods, held in place only through the tension in the string. The tension hook holds the back side of the string loop, allowing straightforward hooking and unhooking by manually bending the rods. Camber impacts the lift distribution around the airfoil, reducing the strength of the leading edge vortices and delaying stall [12]. Its inclusion in the design procedure serve as a tool for future aerodynamic optimization.

Flapping wings without any pitching or twisting provides limited thrust, according to existing models [13], [14], [15]. Pitching can be obtained through a mechanism to rotate the wing, at the cost of increased mechanical complexity [16]. We implement chord-wise flexibility to the wing, inducing a passive pitching movement [17]. For a flapping wing to efficiently move a robot forward, it needs to deform with a 90° phasing [18]. We choose a passive wing structure that elastically deforms through aerodynamic load to achieve this [17]. The flexibility of the trailing edge is dependent upon one main parameter in this design: the diameter of the chord rods. Thanks to the modular design, they can be changed at will. After iteration through varying diameters, we select a 1.5mm chord rod which experimentally yields a large wing deformation, sufficient to permit flight path angles of up to 50 degrees in steady flight. The spar is located at the quarter-chord of the wing as shown in Fig. 2.B. In contrast to a leading-edge spar location, this design choice reduces the torsion loads on the spar and the bending load on the chord-rods, permitting smaller diameters and thus a lighter structure. Additionally, it reduces stresses on the hinge mechanism at the root.

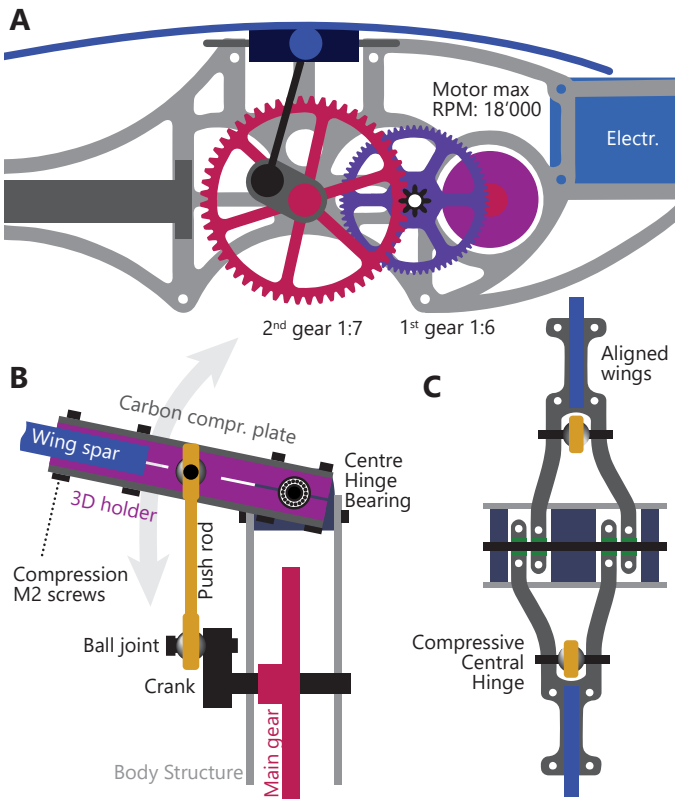

Figure 3. (**A**) Side-view of the transmission, with a reduction of XX. (**B**) Front view of the 4-bar linkage displaying the drive motion of the wings. (**C**) Top view of the Carbon Central Hinge.

B. Tail

Due to the oscillations caused by the flapping of the wings, it is important for the ornithopter to be inherently stable, which means

that the reaction to a perturbation takes the vehicle back to the trimmed state. A tail surface of $0.1\,\mathrm{m}^2$ provides stability as long as the center of mass is not more than $84\,\mathrm{mm}$ behind the center of pressure of the wing.

In addition to providing stability, the tail also serves as an elevator in longitudinal dynamics, whose deflection δ_e fixes the angle of attack during flight. The ability of moving the entire surface of the horizontal tail allows flights at extremely high angles of attack (45º), achieving the high lift needed for slow flight. The frequency ω works as the additional control variable in order to define the longitudinal state, given by $x_{long} = [V,\gamma,\theta,q]^T$ in wind reference frame for conventional aircrafts with V the airspeed, γ the flight path angle, θ the pitch angle and q the pitch angular velocity [19].

A vertical tail provides directional stability. When deflecting the vertical tail by an angle δ_r, a slideslip angle is created, forcing the vehicle to rotate in roll as a consequence of the dihedral angle, which leads to a turn. Therefore, in contrast to conventional aircrafts which have also ailerons, only δ_r controls the lateral state $x_{lat} = [\chi,\phi,\psi,p,r]^T$, where χ is the heading, ϕ and ψ the roll and yaw, and p and r their angular velocities [19].

Both surfaces are actuated at their root with two servos, for pitch control and for rudder control. To improve resolution, and torque, a reduction lever transmission has been designed for each DoF, 2:1 for tail pitch and 1.5:1 for the rudder. The lack of roll actuation on the wing is mitigated by the wing dihedral, which provides lateral stability.

C. Composite Body

The E-Flap's body consists of two CF plate of $1.5\,\mathrm{mm}$ thickness cut to the shape required to house the transmission, the tail, the head and electronics, displayed in light grey in Fig. 3.A. The set of plates, together with bridging $20\,\mathrm{mm}$ spacers, creates a protected space that fully encompasses the entire transmission with the brushless motor slightly protruding on one side. The tail tube is compression-held between inserts, allowing for effortless dismounting and trimming. This is particularly important not only for storage and transport but also for undertaking tail studies, which can be quickly swapped.

The body plates are manufactured from a woven CF flat plate, at a total body cost of under 10$. The profile is cut on a small-scale CNC router with a $2\,\mathrm{mm}$ end mill, making it highly suitable for quick iteration and changes (e.g. new attachment points, center of mass adjustments).

The root of the wings is a failure point and needs careful consideration. Indeed, at the maximum flapping frequency, the drag and inertia will impose vertical loads on the hinge of up to 6.5 Nm. Given a $3\,\mathrm{cm}$ hinge-push rod distance, the maximum forces at the root will be on the order of $200\,\mathrm{N}$. We propose a hinge system that can be entirely manufactured in one hour, and relies on ball bearings for reduced friction. The asymmetric Y-shaped Wing Roots (*dark grey* in Fig. 3.C) are interlaced at the axis of rotation, providing exact alignment of the two wings. The wing can be removed or its pitch angle adjusted in a matter of seconds by loosening the compression screws.

III. Powertrain

This section describes the methodology followed to estimate the power and torque that have led to the sizing of the whole powertrain subsystem.

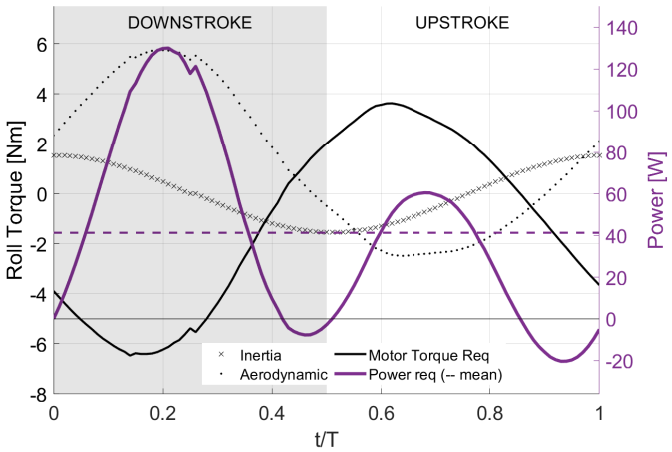

Figure 4. Estimation of the power and torque required from the transmission to fly the E-Flap. Total torque (thick black line) is extracted from component approximation (black lines) and the corresponding power of required from the robot calculated (purple line).

A. Frequency and Stroke estimation

The flapping frequency is estimated using a theoretical, statistical and revised allometrical method for flapping wing micro air vehicles (FWMAVs) sizing [6]. Based on Pennycuick observations and proposed formula [20], Hassanalian's methodology adds a correction factor that depends on the FWMAVs features as follows

$$f = \zeta m^{\frac{3}{8}} g^{\frac{1}{2}} b^{\frac{-23}{24}} S^{\frac{-1}{3}} \rho^{\frac{-3}{8}}, \tag{1}$$

where f stands for flapping frequency, ζ for the correction factor, m for the robot mass, g for the gravity, b for the wingspan, S for the wing surface and ρ for the air density. The correction factor selected ([6] Table 2) is $\zeta = 1.48$, corresponding to the ornithopter with the closest wingspan to the E-Flap, i.e. the Slowhawk. Using Eq. 1 the flapping frequency obtained is $f = 3.687 \approx 4Hz$.

Following Hassanalian's sizing methodology, the next step is to decide the flapping amplitude, which corresponds to the sum of upstroke and downstroke angles. Based on the optimal Strouhal number that provides a peak efficiency [6], S_t = 0.3, and setting the forward speed $v = 5\,\mathrm{m/s}$, the domain of upstroke, h_a, is estimated with (2) left, and (2) right then yields the up/down-stroke angles φ.

$$S_t = \frac{2fh_a}{v}, \qquad \varphi = 2\sin^{-1}\left(\frac{2h_a}{b}\right) \approx 32. \tag{2}$$

The proportions between the components of the 4 bar mechanism determines the flapping angles: amplitude and mean dihedral. The nominal design provides 30-50° amplitude and a 5° positive dihedral. Thanks to the versatile and modular design some of these specifications (i.e. flapping amplitude, dihedral) can be easily altered. For example, manually changing the crank (see Fig. 3.B), which sets the distance between the main gear axis and the ball joint, changes the flapping amplitude to 30°, 40° or 50°. The gear reduction can also be adjusted by selecting the pinion at the motor

B. Torque and Power estimation

The E-Flap's transmission supplies the mechanical power to the wings. The required torque and power are estimated based on an analytical and Computer Fluid Dynamics (CFD) analysis of the wings. The total torque on the transmission M_{TR} is calculated as

$$M_{TR}(\xi) = -M_{aero} + I_{root}\ddot{\xi}, \tag{3}$$

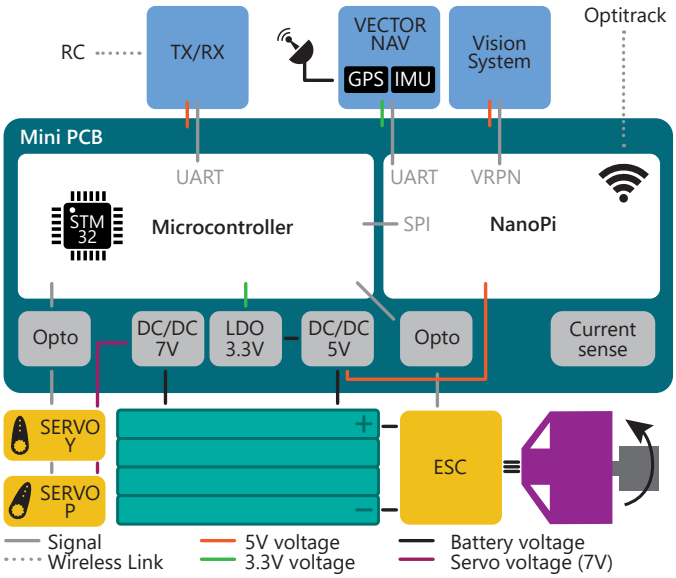

Figure 5. Diagram of the electronic network on-board the flying robot. The mini-PCB interfaces the NanoPi Breakout board with a micro-controller and active components (in gray). Connections are shown in colored lines.

for every angle of the wing with respect to the horizontal body plane $\xi \in [-20,+30]$. The result is shown in Fig. 4

The inertia term I_{cm} is calculated in the CAD software and shifted from the center of mass to the root $I_{root} = I_{cm} + m_{wing} Y_{cm}^2$, where Y_{cm} is the distance from the root to the center of mass of the wing and I_{root} is the equivalent inertia at the flapping axis. The contribution of the inertia is large (as seen in Fig. 4 line 'x'), thus a lightweight wing construction is paramount. The aerodynamic component M_{aero} on the semi-wing is obtained through a CFD simulation. The simulation considers a simplified flapping and pitching wing motion. The wing is approximated as a 1mm flat plate. The CFD was performed with a RANS k-omega model which is typically employed in low Reynolds number situations. The simulation mesh contains 3.5 million elements. The simulation is run over 100 steps within a flapping cycle and convergence is obtained with a 10^{-6} residual. The total torque estimated from those two components is maximum in the middle of the downstroke, reaching $6.5\,\mathrm{Nm}$ as shown in Fig. 4. The power requirement for the full wing is then given by $P = 2 M_{TR} \dot{\xi}$. This estimation does not account for wing elasticity, camber, power transmission losses but does give a starting point for the transmission design.

The large oscillating wings need about 4Hz during cruise flight, which is rather low for the nominal speeds of standard brushless motors. The power requirement of the motor is set by the power estimation above with a safety margin. A 150W motor is selected, capable of supplying the peak power estimation of 130W. A direct transmission to the wings would require a low Kv motor, which tends to be large and heavy. Employing a smaller and faster motor with a reduction gearbox is found to be more efficient in weight. The flapping mechanism is therefore composed of three distinct parts: a 1130Kv brushless motor, a 2-stage gear reducer of 42:1, and the 4-bar linkage that connects the output rotatory shaft with the flapping wings.

IV. Avionics

The flight capability of a flapping-wing device depends on light electronics and adequate control. Autonomous navigation also requires a sensor set interacting with the hardware driver. To this end, we propose a unified electronic system capable of interfacing with all sensors needed for free, autonomous flight, displayed in Fig. 5.

The carrier custom PCB of this system is optimized for minimal weight (10 grams). It carries a micro-controller, power regulation for 6x servos, communication and computation capability with the NanoPi Quadcore which handles perception components (cameras etc..) and connects to state-of-the-art GPS navigation unit and IMU. The STM32 microcontroller soldered on the PCB interprets commands from the NanoPi over SPI and drives the adequate actuators. As well, it handles RC commands for manual flights.

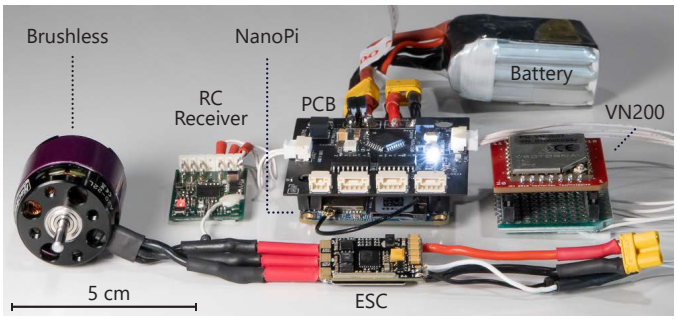

Figure 6. Photo of the on-board electronics.

The power from the battery is split into three buses. The first bus powers the actuators (servos) and is regulated to between 5V and 7V by a TPSM53604 new generation DC/DC regulator. With a 95% efficiency, state-of-the-art small footprint (5.5x5.5 mm) and 4A handling capability, this regulator is ideal for this flying application. A second regulated bus (fixed 5V) powers the on-board computer, RC receiver and vision sensors. Additional regulation further lowers the 5V line to 3.3V for the micro-controller and VectorNAV unit.

The NanoPi companion computer directly plugs into the PCB with the micro-controller, permitting quick swapping. The NanoPi Air Neo is an open source processing board with a $1.2\,\mathrm{GHz}$ quad-core processor. It supports a micro SD, camera connections and features an on-board WiFi module, used to receive flight instruction from and external PC when flying in a tracked space. In this case, the attitude and position of the robot is tracked externally and the control algorithm calculates new commands that are transmitted to the NanoPi and subsequently to the micro-controller and hardware. The NanoPi connects to the VectorNAV VN-200 board. The state-of-the-art chip provides position and inertial data at up to $400\,\mathrm{Hz}$. We choose this solution for its low weight (4g chip), high accuracy and praised processing engine. The NanoPi provides ample processing power for increased autonomy in uncontrolled conditions, which will be the focus of further research articles. The carrier PCB and companion computer stack is designed to fit in the neck of the E-Flap, within the $20\,\mathrm{mm}$ space. This optimal location is protected from impact thanks to the head and composite neck plates and contributes to moving the center of mass forward, improving stability in flight. A PI controller in the pitch angle is implemented for the simple indoor maneuvers performed. This controller is connected to the Optitrack motion capture system using a similar architecture as in [11], and it is used to perform controlled

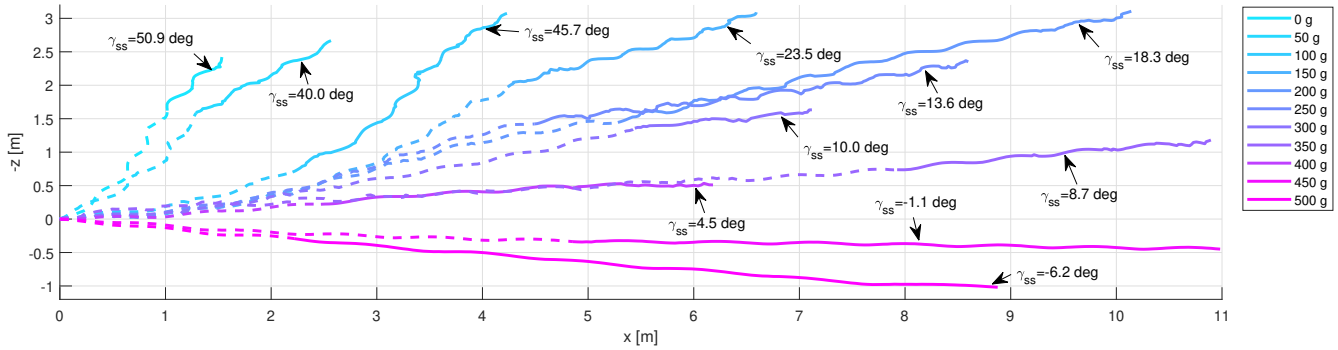

Figure 7. 2D free flight trajectory with pitch controller and with varying payload in increments of 50g. The trajectories are obtained via visual infrared tracking. Dashed lines: initial transient after the launch. Solid lines: portion of the trajectory where the mean value of the flight path angle γ is in steady state. The plot shows that the E-Flap can sustain level flight with a maximum payload of 520g.

maneuvers in indoor flight tests. All the tests are performed with the same controller configuration, since we found experimentally that it performed as expected for different flight conditions.

V. Results

A. Mass and power distribution

The minimal weight of the robot with an autopilot flight configuration is 510 g, including 10 g for tracking electronics. This can be broken down into categories as shown in fig. 8 (left). The flapping engine consists of a brushless motor (20g) and its transmission, weighing a total of 71 grams. Thanks to their light fabrication technique, the wings weigh less than 15% of the total mass, at only 82g. The tail segment includes the two servo actuators (15g each) for the rudder and elevator.

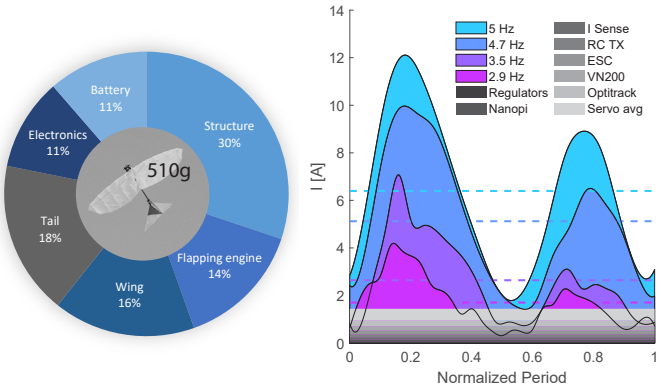

Figure 8. (**Left**). Mass distribution of the Flapping-wing robot. (**Right**) Current consumption at 16.5V of the E-Flap in flight at varying frequencies and with the contribution of all electronic components.

The power consumption of the E-Flap is reported in Fig. 8 (right) at 16V voltage level. The measure is realized on-board with a hall-effect sensor, in free flight. The value is calibrated against a bench top power supply. The on-board electronics (including servo actuation) can use up to 1.5 A depending on the flight configuration. The wing actuation consumption is superior to that value at all flight-permitting frequencies. At maximum throttle, peak power levels can reach close to 12 A or close to 200 W. The 65% mean power difference observed with the estimation (Fig. 4) at 4Hz can be explained from transmission losses, electronics losses and approximation of the calculation.

B. Payload Capability

The E-Flap is a fully featured flapping-wing robot fulfilling all the requirement for autonomous flight. The most critical step towards this objective is the ability to carry relevant payload. Nowadays, a payload of 100 g permits a low degree of autonomy - mostly limited to RGB low-resolution cameras, distance sensors and some computing power. A payload of 200 g can already deliver a high-level autonomy with an event camera, high-end computing board and additional proximity sensors. Additional payload can also serve to increase battery capacity and therefore flight time. An additional 93g of battery capacity has experimentally shown to improve flight time from 5 to 15 minutes, in manual free flight tests.

Fig. 7 shows the robot's trajectory in the XZ plane with increasing weight levels in an indoor, tracking zone which optically tracks infrared LED fitted on the robot via 28 cameras.With this setup, flights up to 520 g of payload have been achieved although at the limit of maneuverability and climb rate. The tests were conducted at a flapping throttle of 100%, corresponding to a frequency of 5.6±0.2Hz and with a 4 cell battery, which are parameters that provides the highest lift capability.

C. Maximum Performance Flight Envelope

The objective is to obtain the flight path angle as a function of the pitch angle in steady state (ss) $\gamma_{ss}(\theta_{ss})$, and the velocity as a function of the pitch angle in steady state $V_{ss}(\theta_{ss})$. This defines the flight envelope for a representative payload of 170 g. To do this, a parametric sweep of the pitch angle in $[10,60]$ deg at 100% of flapping frequency is done using a pitch control loop. This range was chosen such that 60 deg is the maximum reachable pitch angle θ and 10 deg is the pitch angle for horizontal flight. In this case, we consider the steady state variables as the mean value of these variables in a flapping period. The results can be seen in Fig. 9.

It can be seen that the maximum flight path angle is $\gamma_{ss,max} = 40.18$ deg for a pitch angle $\theta_{ss} = 58.92$ deg. The maximum velocity is $V_{ss,max} = 5.63$m/s for a pitch angle $\theta_{ss} = 9.80$ deg, with a maximum climb rate $\dot{z}_{ss,max} = 1.79$ m/s for a pitch angle $\theta_{ss} = 37.86$ deg. The maximum climb rate occurs for an intermediate value of the pitch angle due to the nonlinear relationship $\dot{z}_{ss} = -V_{ss}\sin\gamma_{ss}$. This means that if the climb rate $\dot{z}_{ss}$ is to be maximized, the optimal value of θ_{ss} must be chosen.

It is also important to note that since the flight envelope was obtained using 100% of flapping frequency, any state above the

colored area in Fig. 9 is unreachable, and the maximum values shown before represent the maximum performance for a payload of 170 g. The figure also shows that the controller performs correctly, with a maximum mean error of 3 deg. This can be seen by comparing the experimental values of the mean pitch angle in steady state θ_{ss} with the prescribed reference values.

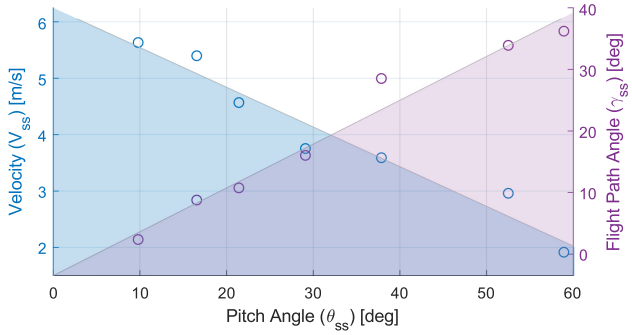

Figure 9. Maximum performance flight envelope at 100% flapping frequency and 170 g payload. The two lines are fitted using the least squares method, and show a linear relationship in steady state. The pitch angle reference inputs for the closed loop tests are [10,15,20,30,40,50,60] deg

D. Wing geometry

One of the design possibilities defined in Subsection II-A is the addition of camber in the forward section of the wing. In this section, we aim to study the influence of camber on flight performance in terms of flight path angle γ. The difference in performance between a flat and cambered wing for three different representative flat wing flight conditions is obtained. The different flight conditions are determined by a constant reference pitch angle (achieved in closed loop), and a fixed throttle (% of the maximum flapping frequency). These conditions are: gliding flight, horizontal flight, and climbing flight. Tail deflection values during the tests are a consequence of the controller acting on the pitch angle to keep it constant. Camber is shown to improve significantly the results at given throttle and control reference. The results are shown in Fig. 10.

At 65% throttle, the cambered wing allows the E-Flap to climb at a flight path angle of 5.89 deg whereas a flat wing at the same throttle only demonstrates level flight. At 70% throttle, the flight path angle for the flat wing of 12.8 deg is improved up to 15.6 deg for the cambered wing. Gliding also show a similar improvement when camber is considered. The glide ratio is improved from 30 deg to 20 deg. This improvement is caused by two factors. First, a cambered airfoil maximizes its lift coefficient (section II-A). Secondly, the camber increases the tension in the wing fabric, reducing the drag that wrinkle causes. Further aerodynamic studies should be performed to optimize the camber amount.

E. Lateral-Directional Maneuverability

Here we examine the lateral-directional maneuverability of the ornithopter. It is quantified via the modulus of the maximum turning rate Ψ_{max}, obtained from the instantaneous center of curvature of a trajectory, for a successful controlled level turn. The turn is done by controlling the heading angle using the vertical tail deflection and the pitch angle using the horizontal tail deflection. The level condition is achieved by controlling the flight path angle in open loop through the pitch angle with a pitch reference of $\theta_{ref} = 20$deg

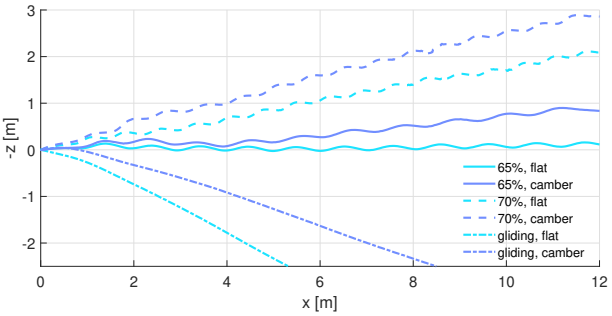

Figure 10. 2D Optitrack trajectories comparing cambered and flat wing. The three representative flight conditions (throttle, reference pitch angle) are: (0%, −10 deg), (65%, 20 deg), (70%, 35 deg).

at 65 % flapping frequency. The maximum turning rate Ψ_{max} is obtained from the Optitrack data.

The results for a test showing the maximum turning rate Ψ_{max} can be seen in Fig. 11. The E-Flap robot is thrown with an initial heading angle $\chi_0 = 50°$. It can be seen that $\Psi_{max} = 2.08$rad/s. The mean flight path angle during the test $\gamma_{mean} = -0.05°$, which is representative of a horizontal flight with constant altitude. This figure also shows the attitude , i.e., yaw, pitch, and roll, for this same test. A comparison between the yaw and roll angles with the trajectory in the horizontal plane (x,y) suggests that the roll is more correlated with the followed trajectory. As a consequence, an improvement in the design to add a control variable for the roll angle instead of the vertical tail deflection should be considered.

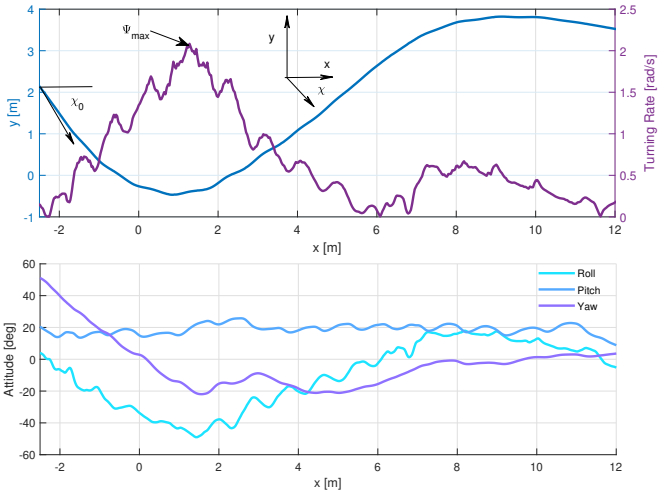

Figure 11. Lateral-directional maneuver for maximum turning rate. The figure shows the trajectory in the horizontal plane (x,y), and the turning rate as a function of space $\Psi(x)$. Data tracked by the Optitrack motion capture system.

F. Outdoor Free Flight

The design and electronics are also validated by performing several outdoor manual flights with GPS/IMU flight data recording. It is shown that the vehicle can be flown safely, record inertial flight data, all in a repeatable way, i.e., the design is sufficiently robust to perform several sustained flights with data logging. More than 100 outdoor manual flight tests have been conducted. The ornithopter is always launched by hand proving safe operation, in contrast to multirotors. It is also easily piloted in calm outdoor atmospheric flight conditions. The wing flapping is displayed in Fig. 12 at

Figure 12. Composite image of the E-Flap along a flapping cycle during outdoor flight.

various positions within a stroke. A typical recorded trajectory using the VN200 is shown in Fig. 13, starting in position 0 (light blue). The trajectory is recorded in the geodetic LLA reference frame at 90 Hz, and then converted to a local NED reference frame, with the origin at the initial position.

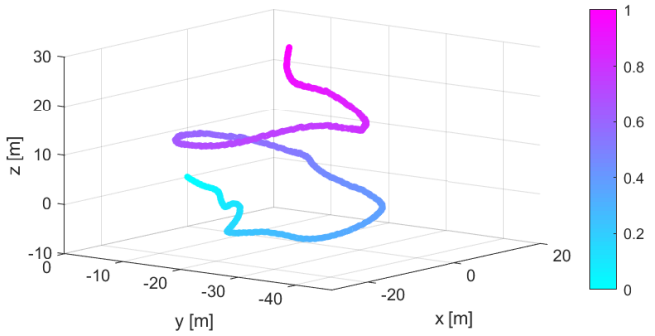

Figure 13. 3D outdoor trajectory from GPS data. The color bar represents the normalized time.

VI. Conclusions

This article presents a novel, payload-capable flapping robot. Such robots show high potential of efficient and safe operation due to the lack of high-speed blades found in propellers. This research brings us a major step forward towards a fully autonomous flapping-wing robot. An overview of the E-Flap robot is presented in this research article, highlighting the driving aspects of aerodynamics, dynamics, mechanical and electronics design. The validity of the concept is verified through numerous experiments. These tests demonstrate a high flapping frequency of up to 5.5Hz a, high pitch angles of up to 70° and a payload capability of up to 520 g, sufficient for flight with the sensors required for full autonomy. As well, full flight capability is shown both indoors and outdoors during over 100 flights. Last but not least, the whole design is built to be manufactured cheaply and quickly with standard 3D printing technology and a 2D plate cutter. This permits a full robotic bird assembly in two days as well as simple part replacements in the field.

Future work will leverage this modular platform to study and demonstrate increasingly complex behavior, including perching, obstacle avoidance, manipulation and interaction with humans. We are already leading research in camera vision, control and physical interaction with several copies of the new E-Flaps, with promising early results. We are expecting to demonstrate closed-loop outdoor flights soon, not only with GPS/IMU but also supplemented with vision sensors and on-board image processing.

References

[1] R. Malka, A. L. Desbiens, Y. Chen, and R. J. Wood, "Principles of microscale flexure hinge design for enhanced endurance," in *2014 IEEE/RSJ International Conference on Intelligent Robots and Systems*. IEEE, 2014, pp. 2879–2885.

[2] H. V. Phan, S. Aurecianus, T. Kang, and H. C. Park, "Kubeetle-s: An insect-like, tailless, hover-capable robot that can fly with a low-torque control mechanism," *International Journal of Micro Air Vehicles*, vol. 11, p. 1756829319861371, 2019.

[3] A. Ramezani, X. Shi, S.-J. Chung, and S. Hutchinson, "Bat bot (b2), a biologically inspired flying machine," in *2016 IEEE International Conference on Robotics and Automation (ICRA)*. IEEE, 2016, pp. 3219–3226.

[4] M. Keennon, K. Klingebiel, and H. Won, "Development of the nano hummingbird: A tailless flapping wing micro air vehicle," in *50th AIAA aerospace sciences meeting including the new horizons forum and aerospace exposition*, 2012, p. 588.

[5] W. Yang, L. Wang, and B. Song, "Dove: A biomimetic flapping-wing micro air vehicle," *International Journal of Micro Air Vehicles*, vol. 10, no. 1, pp. 70–84, 2018.

[6] M. Hassanalian, A. Abdelkefi, M. Wei, and S. Ziaei-Rad, "A novel methodology for wing sizing of bio-inspired flapping wing micro air vehicles: theory and prototype," *Acta Mechanica*, vol. 228, no. 3, pp. 1097–1113, 2017.

[7] J. Gerdes, A. Holness, A. Perez-Rosado, L. Roberts, A. Greisinger, E. Barnett, J. Kempny, D. Lingam, C.-H. Yeh, H. A. Bruck *et al.*, "Robo raven: a flapping-wing air vehicle with highly compliant and independently controlled wings," *Soft Robotics*, vol. 1, no. 4, pp. 275–288, 2014.

[8] A. Perez-Rosado, H. A. Bruck, and S. K. Gupta, "Integrating solar cells into flapping wing air vehicles for enhanced flight endurance," *Journal of Mechanisms and Robotics*, vol. 8, no. 5, 2016.

[9] G. A. Folkertsma, W. Straatman, N. Nijenhuis, C. H. Venner, and S. Stramigioli, "Robird: a robotic bird of prey," *IEEE robotics & automation magazine*, vol. 24, no. 3, pp. 22–29, 2017.

[10] Festo. Smartbird-bird flight deciphered. [Online]. Available: https://www.festo.com/group/en/cms/10238.htm

[11] F. J. Maldonado, J. A. Acosta, J. Tormo-Barbero, P. Grau, M. M. Guzmán, and A. Ollero, "Adaptive nonlinear control for perching of a bioinspired ornithopter," in *Proceedings of the 2020 IEEE/RSJ International Conference on Intelligent Robots and Systems (IROS)*, 2020.

[12] W. Thielicke and E. J. Stamhuis, "The influence of wing morphology on the three-dimensional flow patterns of a flapping wing at bird scale," *Journal of Fluid Mechanics*, vol. 768, p. 240–260, 2015.

[13] I. E. Garrick, "Propulsion of a flapping and oscillating airfoil," *Technical Report TR 567, NACA*, 1936.

[14] M. F. Platzer, K. D. Jones, J. Young, and J. C. S. Lai, "Flapping wing aerodynamics: Progress and challenges," *AIAA Journal*, vol. 46, no. 9, pp. 2136–2149, 2008.

[15] A. J. Smits, "Undulatory and oscillatory swimming," *Journal of Fluid Mechanics*, vol. 874, pp. 1–44, 2019.

[16] G. A. Folkertsma, W. Straatman, N. Nijenhuis, C. H. Venner, and S. Stramigioli, "Robird: a robotic bird of prey," *IEEE robotics & automation magazine*, vol. 24, no. 3, pp. 22–29, 2017.

[17] J. D. DeLaurier, "The development of an efficient ornithopter wing," *The Aeronautical Journal (1968)*, vol. 97, no. 965, p. 153–162, 1993.

[18] S. Heathcote and I. Gursul, "Flexible flapping airfoil propulsion at low reynolds numbers," *AIAA journal*, vol. 45, no. 5, pp. 1066–1079, 2007.

[19] B. L. Stevens, F. L. Lewis, and E. N. Johnson, *Aircraft control and simulation: dynamics, controls design, and autonomous systems*. John Wiley & Sons, 2015.

[20] C. Pennycuick, "Wingbeat frequency of birds in steady cruising flight: new data and improved predictions," *Journal of Experimental Biology*, vol. 199, no. 7, pp. 1613–1618, 1996.